



HAL
open science

Oil Films Characterization from X-to K-band, a Wind-wave-pool Experiment

Aymeric Mainvis, Vincent Fabbro, Christophe Bourlier, Henri-Jose Mametsa,
Pierre Borderies

► **To cite this version:**

Aymeric Mainvis, Vincent Fabbro, Christophe Bourlier, Henri-Jose Mametsa, Pierre Borderies. Oil
Films Characterization from X-to K-band, a Wind-wave-pool Experiment. 2020. hal-02468217v1

HAL Id: hal-02468217

<https://hal.science/hal-02468217v1>

Preprint submitted on 5 Feb 2020 (v1), last revised 28 Jul 2020 (v2)

HAL is a multi-disciplinary open access archive for the deposit and dissemination of scientific research documents, whether they are published or not. The documents may come from teaching and research institutions in France or abroad, or from public or private research centers.

L'archive ouverte pluridisciplinaire **HAL**, est destinée au dépôt et à la diffusion de documents scientifiques de niveau recherche, publiés ou non, émanant des établissements d'enseignement et de recherche français ou étrangers, des laboratoires publics ou privés.

Oil Films Characterization from X- to K-band, a Wind-wave-pool Experiment

Aymeric Mainvis*, Vincent Fabbro†, Christophe Bourlier‡, Henri-Jose Mametsa§ and Pierre Borderies¶

*†§¶ONERA/DEMR, Université de Toulouse, F-31055 Toulouse France

‡IETR, Polytech Nantes, Nantes France

Email: *Aymeric.Mainvis@onera.fr, †Vincent.Fabbro@onera.fr, ‡christophe.bourlier@univ-nantes.fr,

§Henri-Jose.Mametsa@onera.fr, §Pierre.Borderies@onera.fr

Abstract

This paper depicts an experiment conducted in a wind-wave pool in Brest, France, to characterize oil films when observed at moderate incidence from a X-to-K-band radar. Simultaneous measurements of surface elevation and radar backscattered field were carried out for various sea water surface states and incident angles. From this meaningful dataset (mainly lying in simultaneous acquisitions in X-, Ku- and K-band), an inversion method is proposed to characterize some properties of the oil film: its origin (mineral or biogenic) and its fractional coverage indicator. This process is based on the minimization of the cost function correlating the values given by a physical model of the wave damping ratio and the measured ones. The resulting oil parameters are found in overall good agreement with the three different released oils (two mineral and one biogenic) and it is observed that the fractional filling indicator of the oil slick decreases with increasing the roughness surface state whatever the considered oil.

Index Terms

radar scattering, sea surface electromagnetic scattering, ocean remote sensing, oil slicks, water pollution, inversion method

I. INTRODUCTION

Both civil authorities and oil companies make use of either spaceborne or airborne remote sensing sensors to monitor hydrocarbons in an offshore context [1], [2]. This maritime activity relies, in particular, on preventing boats from illegal fuel releases and on tracking incidents. This global monitoring is also applied in the prospection domain to identify natural occurrence of crude oils on the ocean surface and then, potential natural crude oil tank under the seafloor [3]. Currently, Synthetic Aperture Radar (SAR) is the main system to detect hydrocarbons on sea surfaces [4], [5], [6]. This approach is preferred for weather-and-time-related issues, ensuring an anytime ready system. Electromagnetic (EM) waves are sensitive to the sea surface roughness variations induced by the presence of oil films. Precisely, the latter dampens the short sea waves by both suppression of wave growth and increase in wave dissipation [7]. This phenomenon implies zones of reduced backscatter in the SAR image which makes the presence of hydrocarbons detectable in radar imagery. Many studies have been achieved to further develop

hydrocarbons detection strategies in an ocean context [1], [2], [8]. Furthermore, a recent overview of the radar parameters to detect oil film is proposed and suggests a relative efficient-oriented classification [9].

However, in a global maritime environment supervision, identifying oil-covered ocean areas is not enough. The characterization of the detected product is a key element in the decision making process for economic purposes or clean-up operations. To address this issue, optical hyperspectral imaging is commonly used [10] but remains unsatisfying in an operational monitoring context. Achieving this characterization through radar signals would be a great improvement for the supervision of oil slicks. The radar signature of an oil-covered ocean surface has been tackled by many studies [11], [12], [13], [14], [15], [16] and [17]. Literature depicts this particular signature thanks to theoretical models and experimental measurements from C- to Ka-band in both dual-polarization and cross-polarization. Precisely, the oil film (either mineral or biogenic) is studied by observing the wave damping effect.

Motivated by the previous analysis (summed up in [7]) about the impact of the wave damping effect on the radar damping ratio (which is the ratio between clean ocean surface radar signature and oil-covered one), this paper addresses the oil characterization feasibility by using multi-frequency and multi-polarization data for a given illuminated controlled oil-covered sea water surface. The originalities of this paper lie, firstly, in the achieved experiment providing multi-parametric, multi-acquisition-mean and controlled-environment data of three different oils, two mineral ones: crude oil and gasoil ; and a biogenic one: colza oil. The parameters are the surface state, the incident angle, the radar frequency and the polarization. Moreover, the sea water surface –controlled thanks to the axial fans, the wind-wave pool and the continuous oil injection over the surface– is characterized by two different systems, the radar system and the high-resolution capacitance wave probes. Secondly, an original method is investigated to retrieve the wavenumber height sea water surface spectrum from the wave probes data. At last, the use in the oil characterization strategy of a physical modeling of the backscattered EM signal and the impact of oil on the surface is combined with a cost function minimization to estimate *a priori* oil film chemical parameters.

This paper is organized as follows: Section II describes the experimental setup, it is composed of the wind-wave pool, the radar system and the high-resolution capacitance wave probes. The basic statistical parameters of the observed wind wave fields are derived in section III. Section IV details the radar measurement by introducing the collected database and the procedures to perform measurements of both the EM incoherent field, the radar cross section (RCS) and the damping ratio. In Section V the proposed methodology to characterize the oil film is tested. Results of the proposed characterization method are displayed in section VI and section VII is devoted to summary and outlooks.

II. EXPERIMENTAL SETUP

The experiment is carried out in a pool at the CEDRE¹ in Brest, France. The pool is a 20-meter-long, 11-meter-wide and 2-meter-deep sea water tank as represented in Fig. 1a. The steady winds are generated thanks to two axial fans sequentially used, one with unique delivered power and the other with an adjustable delivered power

¹Centre of Documentation, Research and Experimentation on Accidental Water Pollution

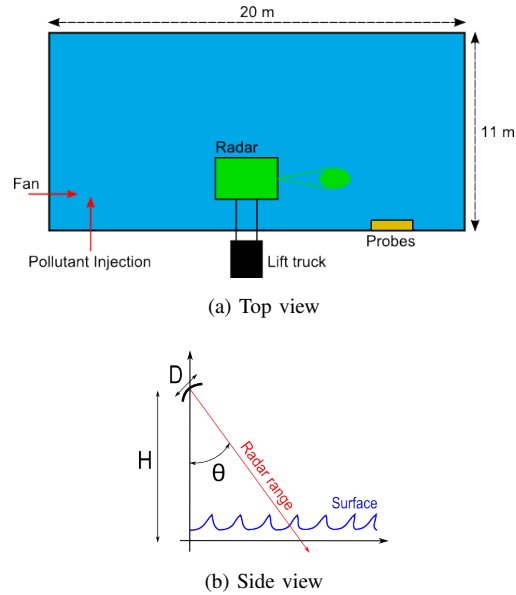


Fig. 1. Schematic view of the experimental configuration and the instrumentation set up

(respectively constant and variable established windspeed over the sea water surface).

The radar system is set up at a fixed position situated at 9 m from the left side of the pool in Fig. 1a. It is plugged on two rotating plates, each one driven by a step-by-step engine (allowing inclinations up to $\pm 45^\circ$ away from nadir and possibly sweeping $\pm 180^\circ$ in azimuth). The RF signal –both the source and the receiver– is provided by a four-port vector network analyzer (VNA²). The antenna is a paraboloid one described in [18], its shortest dimension is $D = 40$ cm and a multipolarized source is located at its focus (cf. Fig. 1b). In laboratory conditions, for the given antenna and for the considered radar frequencies (that are X-, Ku- and K-bands), the far-field-region condition is not achieved. Thus, the radar measurements are operated in the near-field region, which induces a constant incident angle over the radar beam footprint. At nadir, the antenna is situated at $H = 2.3$ m above the sea water surface. At this elevation and by considering an incident angle θ , the divergence of the beam can be neglected for the Ku- and K-band and the electric field distribution is assumed to be uniform over the aperture. Indeed, the Fresnel zone starts at $D^2/2\lambda_0 \approx 3.20$ m with λ_0 the radar wavelength for a frequency of 12 GHz. This distance is qualitatively similar to $H/\cos\theta \approx 3.25$ m for $\theta = 45^\circ$. Furthermore, by considering an incident angle of 25° , this value becomes 2.54 m, which is less than the Fresnel zone distance at frequencies greater than 12 GHz. In the X-band configuration, the radar system operates in the limit of the Fresnel zone. However, the antenna is composed of a high precision offset parabolic reflector, avoiding the divergence of the near-field beam in this controversial band. This is confirmed by the measurements of the normalized incoherent field with range that are similar from 8.5 up to 23.5 GHz (cf. Appendix A). Radar absorbing materials conveniently placed avoid spurious reflections provided by an other element of the experimental environment than the sea water surface. At last, the overall RF system is installed on a lift truck.

²ZVA from Rhode & Schwarz

The geometrical properties of wind waves during radar measurements are estimated thanks to seven high-resolution capacitance wave probes (Fig. 2). Each sensor is made of two sensitive wires hung vertically by a plastic prop and fixed with a wood interface at the pool edge [19]. The probes are aligned in the vertical radar range plan and they measure continuously the voltage variations –linked to the surface wind waves through a calibration process– with a temporal resolution of 1.0 ms.

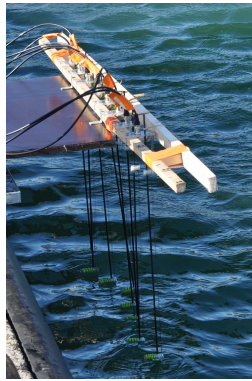


Fig. 2. View of the wave probes

III. SURFACE ELEVATION MEASUREMENT

The surface elevation measurements are made for a period corresponding to a steady wind wave generation over the sea water surface and during one minute to get short- and long-period wind waves.

The high-resolution capacitance wave probes record the temporal voltage variations. This electric tension can be converted into an altitude thanks to a linear regression between voltage and altitude. So, the calibration consists in the measurement of the voltage for different known depth points. From this calibration series of measurements, the linear coefficients are fitted.

From the temporal wind waves profile, the surface state can be statistically characterized by assuming that the sea water surface elevation is a stationary ergodic process. In particular, the mean frequency height sea water surface spectrum (that is the Fourier transform of the autocorrelation function of the temporal wind waves profile) and the standard deviation of the surface height σ_h can be estimated. These two quantities are fundamental in this paper. σ_h is a relevant parameter since it is directly linked to the significant wave height of a sea surface $H_s = 4\sigma_h$ and the frequency spectrum characterizes the temporal structure of the sea water surface. Here, three wind waves generation scenarios are experimented, leading to three different standard deviations of the surface height: 0.282 cm, 0.684 cm and 1.09 cm. These values are the references to quantitatively identify the structure of the sea water surface. Fig. 3 shows an example of a surface elevation measurement considering the first wind waves generation scenario, that is a standard deviation of the surface height of 0.282 cm.

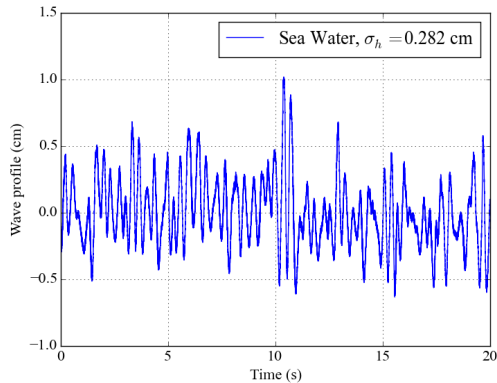


Fig. 3. Example of wind waves profile measurement versus time. The standard deviation of the surface height is 0.282 cm.

IV. RADAR MEASUREMENT

A. Overview of the database

For a given sea water surface state, the studied pollutant is progressively and continuously injected on the sea water surface. The radar measurements are performed in downwind configuration at two possible incident angles (25° and 45°) in monostatic configuration and at preselected frequency bands for co-polarizations (horizontal and vertical). The radar system is monitored by a PC –thanks to a program in Python language– controlling the motors for the antenna positioning and the VNA through an ethernet link. The main conditions are summed up in Table I.

TABLE I
SYNTHESIS OF PERFORMED RADAR MEASUREMENTS AND ASSOCIATED CONDITIONS

Product	Surface State (σ_h cm)	Incident Angle ($^\circ$)	Band
Sea Water	0.282; 0.684; 1.09	25; 45	X, Ku, K
Colza Oil	0.282; 0.684; 1.09	25; 45	X, Ku, K
Crude Oil	0.282	45	X, Ku
Gasoil	0.684; 1.09	25; 45	X, Ku, K

B. Measurement of the Incoherent Field

The sea water surface is a specific radar target. Indeed, to measure such a moving target, the latter has to be considered as static during the measurement time. Transmission and reception of a continuous electromagnetic wave are achieved through the S11 and S12 ports of the VNA. Classically, to obtain range discrimination, a frequency ramp is emitted and the complex backscattered data are transformed to the time domain with the Fourier transform. For each frequency, the time measurement duration is of order $1/B$ with B the intermediate frequency (IF) filter width. Here, the IF filter width is 100 kHz, then each radar acquisition duration is about $10 \mu\text{s}$ and the illuminated scene is assumed static during this time of acquisition. Actually, the processing in range involves a set of frequencies which corresponding acquisition time is still fast enough so that the emitter-receiver sees a

motionless scene. To provide data in the three considered frequency bands, the total EM backscattered field is measured for every frequency component in the frequency ramp of the radar pulse signal (7274 frequency steps from 8.0 to 24.0 GHz). The data are then transformed to time domain in 1-GHz sub-bands and coherently averaged, assuming that the change of incoherent backscattered field (that is the variance of the total field) resulting from the variation of frequency is negligible for such a radio frequency bandwidth and that the sum of time measurements for each frequency sub band does not exceed the backscattered field temporal coherence. In other words, the last assumption suggests a backscattered field temporal coherence greater than 4.55 ms, which is consistent with [21]. The total field is estimated from 500 successive measurements separated in time by 1.5 s, assuming that the sea water surface elevation at each measurement corresponds to an independent realization of the same random process. This assumption is true when the time lag is of the order of few seconds, duration much larger than the period of dominant waves [20]. At last, in this process, echoes from potential static targets are directly filtered; they have no variance in time. Fig. 4 plots the incoherent backscattered field versus the radar range with an incident angle $\theta = 45^\circ$ in VV polarization at 10.5 GHz. The red color line is the incoherent backscattered field of the sea water surface with the sea water state $\sigma_h = 0.282$ cm. The blue dashed line is the one of the sea water surface when the fan is not powered, that is the one of a flat sea water surface. Then, the measured sensitivity is 18 dB. Typically, with the sea water state $\sigma_h = 0.282$ cm and at an incident angle $\theta = 45^\circ$, the measured sensitivity is varying from 5 dB in HH polarization at 23.5 GHz to 21 dB in VV polarization at 8.5 GHz. This value is even greater when higher sea water states and/or smaller incident angles are considered.

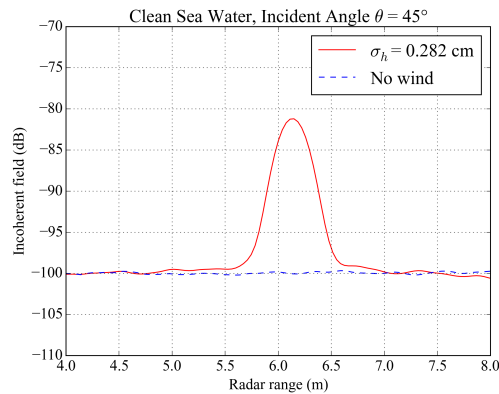


Fig. 4. Incoherent field versus the radar range considering a clean sea water surface with an incident angle $\theta = 45^\circ$ in VV polarization. Two configurations are observed: a sea water state $\sigma_h = 0.282$ cm (red line) and a flat sea water surface (blue dashed line)

C. Measurement of the Damping Ratio

The damping ratio β is defined as the ratio between the RCS of a clean sea water surface σ_c and the one of a polluted surface σ_p , that is $\beta = \sigma_c / \sigma_p$. The RCS is proportional to the intensity of the incoherent backscattered field. More precisely, it corresponds to the mean value of the incoherent backscattered field over the radar beam footprint on the sea water surface [20]. To get a measurement statistically representative of the random sea water

surface elevation, the footprint size has to be much larger than the dominant wavelength of the studied surface. In experimental conditions, the footprint size S_p is constrained –in near-field configuration– to $S_p = D / \cos \theta$ with $D = 40$ cm the antenna diameter. That is ≈ 44.1 cm for $\theta = 25^\circ$ and ≈ 56.6 cm for 45° . However, the missing large scales are included through their tilting effect in the time-averaging process of the backscattered field [20]. Fig. 5 shows an example of measured damping ratios from gasoil slick considering two different sea water states

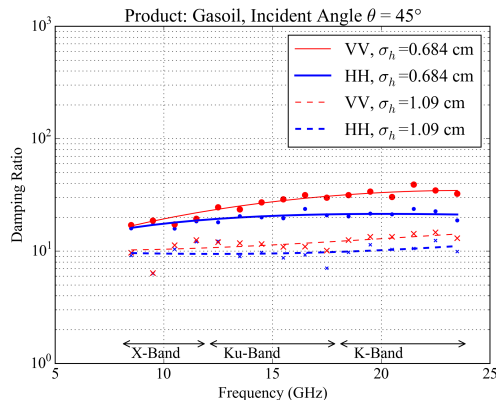


Fig. 5. Damping ratios calculated from gasoil slick acquired at two different sea water states both in VV (red) and HH (blue) polarizations at an incident angle of 45° . The lines are third-degree-polynomial fits on the acquired data points (dots and crosses).

in VV and HH polarizations at an incident angle of 45° . One can observe that the damping ratio increases from X- to K-band, it is poorly impacted by the polarization and decreases with increasing the sea water state. These observations are in agreement with those summed up by Holt and Jones [7].

V. OIL SLICKS CHARACTERIZATION

A. Overview of the methodology

The objective is to correlate the measured damping ratios with an oil slick characterization. To do this, the suggested approach is based on the Bragg scattering mechanism and on the modeled wave damping ratio expression proposed by Lombardini et al. [12]. In the Bragg scattering regime, the RCS can be expressed as the multiplication between the Bragg kernel –corresponding to an effect mainly driven by the polarization and the dielectric characteristics– and the wavenumber height sea water surface spectrum. This asymptotic formalism is called the first order small perturbation method (SPM1) [22]. The modeled wave damping ratio is applied to the wavenumber height clean sea water surface spectrum to characterize the damping effect provided by a given oil slick. In this modeled ratio, three main parameters are used to describe the oil film: the elasticity modulus E_0 in N/m, the characteristic frequency ω_D in rad/s and the fractional filling factor F . So, the methodology is as follows: to validate the Bragg scattering mechanism, the wavenumber height clean sea water surface spectrum is derived from the temporal surface elevation measurements. Then, by using this spectrum, the backscattering normalized radar cross section (BNRCS) is computed from two electromagnetic models, that are the first order small slope approximation (SSA1) [23] and SPM1. SSA1 can be applied from nadir (0°) to moderate incident

angles (up to 70°) [24]. SPM1 is relevant for moderate incident angles only (from 45° to 70°), where the Bragg theory describes the scattering process. When the two approaches produce the same results in term of BNRCS, then the SPM1 is valid and the Bragg scattering regime is established. If Bragg scattering regime is established, and under some approximations discussed later in the paper, the damping ratio can be directly derived from the BNRCS ratio between clean and contaminated sea surface. Afterwards, a cost function minimization is performed on the measured damping ratios to get the three parameters $\{\omega_D, E_0, F\}$ from the modeled damping ratio expression.

The overall strategy is summed up in Fig. 6. The steps *Elevation Measurements* and *Wavenumber Spectrum*, detailed in V-B, stand for the wavenumber height clean sea water surface spectrum estimation from the temporal surface elevation measurements. *Bragg Scattering Demonstration* and *SSA1, SPM1*, explained in V-C, address the validation of the Bragg scattering mechanism and *Damping Ratio Model*, in V-D, deals with the modeled wave damping ratio. At last, *Cost Function Minimization* –in V-E– is the inversion strategy to retrieve the *Characterization Parameters* of the oil films in section VI.

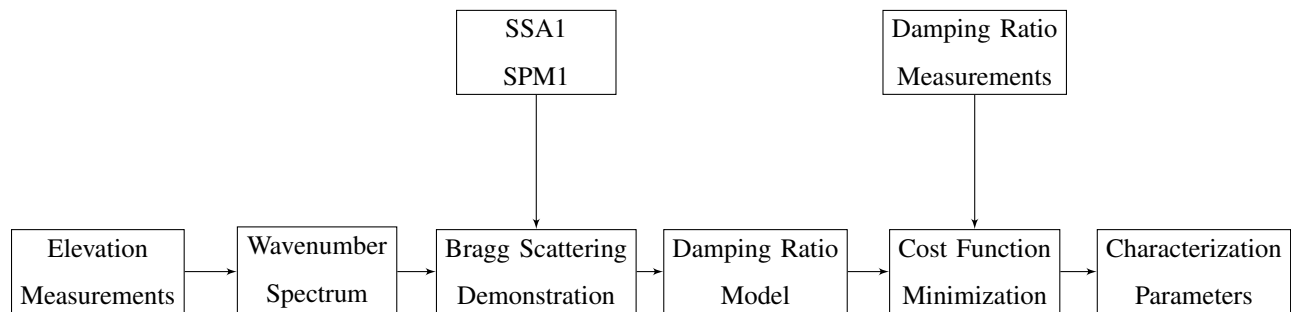


Fig. 6. Schematic diagram of the methodology

B. Frequency to Wavenumber Conversion: Height Sea Water Surface Spectrum

From the temporal surface elevation measurements, the mean frequency height sea water surface spectrum S_f can be computed for each sea water surface state. It is performed as follows,

$$S_f(\omega) = \langle |A(\omega)|^2 \rangle, \quad (1)$$

with $\langle \dots \rangle$ the average over the seven wave probes, A the Fourier transform of the seven wind wave profiles and $\omega = 2\pi f$, f the frequency of the sea water surface waves. However, the state-of-the-art electromagnetic scattering models –SSA1 and SPM1 in particular– make use of the wavenumber spectrum and not the frequency one. Therefore, a frequency-to-wavenumber conversion has to be undertaken. The relation between the frequency spectrum S_f and the wavenumber one S_k is [25]

$$S_f(\omega)d\omega = S_k(k)dk, \quad (2)$$

with k the surface wavenumber. Then, performing the conversion is reduced to the estimation of the group velocity $V_g = d\omega/dk$. The group velocity can be directly derived from the dispersion relationship for long and short waves in an ocean context,

$$\omega^2 = gk \left[1 + \frac{k^2}{k_m^2} \right], \quad (3)$$

with g the acceleration due to gravity and $k_m = 370$ rad/m [25]. To apply this expression to the considered experimental context, the actual group velocity is measured and then compared to that obtained by the dispersion relationship (3). The propagation time delay τ_{nm} between two probes n and m spaced by the known distance d_{nm} is estimated thanks to R , the cross-correlation of the two temporal wind waves profiles h_n and h_m recorded by the probes,

$$R(\tau_{nm}) = \max \left[\text{FT}^{-1} \left[\text{FT}(h_n) \text{FT}^*(h_m) \right] \right], \quad (4)$$

with FT the Fourier transform, FT^{-1} the inverse Fourier transform and \cdot^* the complex conjugate. Then, this delay is compared with τ_{nm}^e , the one calculated by applying the dispersion relationship to compute the theoretical cross-correlation \mathcal{R} ,

$$\mathcal{R}(\tau_{nm}^e) = \max \left[\text{FT}^{-1} \left[\text{FT}(h_n) \text{FT}^*(h_m) e^{jk(\omega)d_{nm}} \right] \right], \quad (5)$$

with $k(\omega)$ the dispersion relationship (3). Here, a two-dimensional problem is considered. Arguably, the wind waves generation process through the axial fan (Fig. 1a) leads to mono-directional wind waves, and so, the crosswind variations are disregarded. Fig. 7 plots the dispersion relationship calculated from the sea water surface state

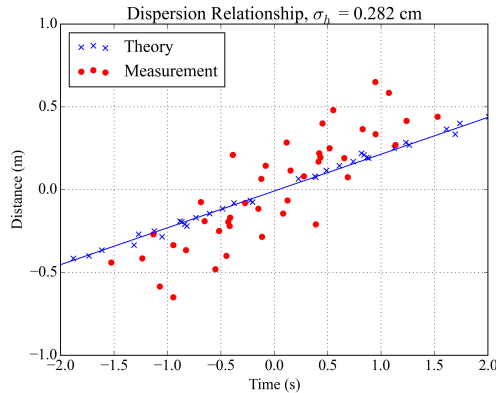


Fig. 7. Dispersion relationship calculated from the sea water surface state $\sigma_h = 0.282$ cm in theory (5) (blue color) and according to measurements (4) (red color). The continuous lines are linear fits on the data points (red dots and blue crosses).

$\sigma_h = 0.282$ cm in theory and according to measurements. Despite a variability in the measurements, the ocean-context dispersion relationship applied to the considered experimental situation remains in correct agreement with the actual measured one. Then, in what follows, the ocean-context dispersion relationship (3) is used to perform the frequency-to-wavenumber conversion and so to compute the wavenumber height sea water surface spectrum. An example is displayed in Fig. 8, the behaviour in $1/k^3$ –commonly found in ocean spectrum modelings like the Elfouhaily model [25]– is retrieved in the wavenumber interval $[1, 100]$ rad/m. Above the wavenumber 100 rad/m, the

capillarity regime is largely energetic with different variations along the wavenumber track. At last, the wavenumber identifying the dominant surface waves is 0.3 rad/m, this value matches the time period 3 s by applying the dispersion relationship (3). This time period is then of the order of the time lag in the radar measurement process, that is 1.5 s.

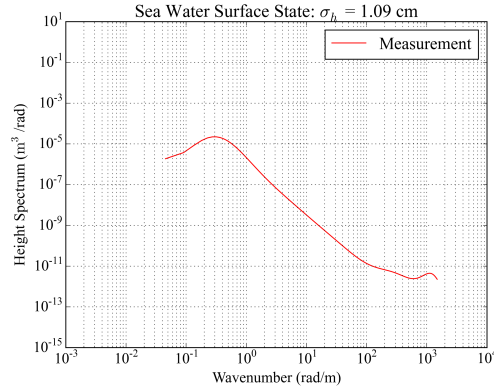


Fig. 8. Wavenumber height sea water surface spectrum computed from the sea water surface state $\sigma_h = 1.09$ cm.

C. Bragg Scattering Mechanism

The Bragg theory predicts that the BNRCS is proportional to the spectral energy density of the Bragg waves, that are the sea surface waves of wavenumber k_B [15],

$$k_B = 2k_0 \sin \theta, \quad (6)$$

with $k_0 = 2\pi/\lambda_0$ the radar wavenumber, λ_0 the radar wavelength and θ the incident angle. Then, by considering a clean sea water surface, the BNRCS σ_0 can be written as [26]

$$\sigma_0(k_0, \theta) = \frac{1}{4k_0} |\mathbb{B}(k_0, \theta)|^2 S_k(k_B), \quad (7)$$

with $\mathbb{B}(k_0, \theta)$ the first order small perturbation model kernel [22] (a term driven by the polarization and the dielectric characteristics) and S_k the measured wavenumber height clean sea water surface spectrum. However, this theory is valid for moderate incident angles only. To verify the applicability of this theory in the considered experimental conditions, a second –more accurate– model is used, that is the SSA1 introduced by Voronovich et al. [23]. According to Voronovich et al., the scattering operator for a two-dimensional sea water surface elevation $\eta(r)$ is given by

$$\mathbb{S}(k_0, \theta) = \frac{\mathbb{B}(k_0, \theta)}{Q_z} \int_r e^{-jQ_z \eta(r)} e^{-jk_B r} dr. \quad (8)$$

The generated sea surface induces a limited integration length in (8) and it leads to the modified scattering operator

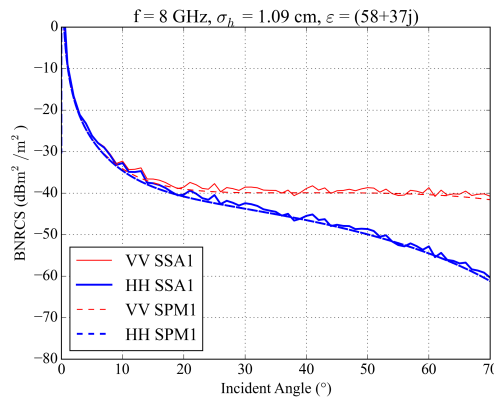
$$\mathbb{S}_{mo}(k_0, \theta) = \frac{\mathbb{B}(k_0, \theta)}{Q_z} \int_{-L/2}^{+L/2} e^{-jQ_z \eta(r)} e^{-jk_B r} dr, \quad (9)$$

with L the effective illuminated length. Then, the BNRCS of a finite surface σ_0 is expressed as

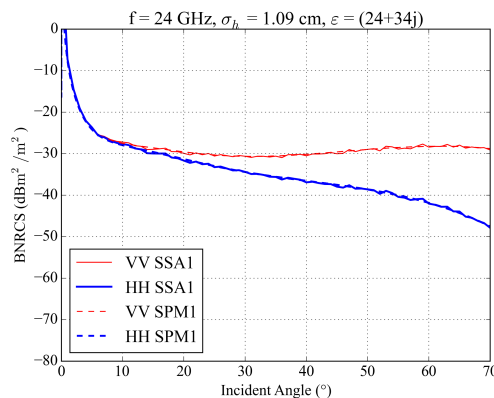
$$\sigma_0 = \frac{\langle \mathbb{S}_{mo} \mathbb{S}_{mo}^* \rangle}{4k_0 L} = \frac{\langle \mathbb{S}_{mo} \rangle \langle \mathbb{S}_{mo} \rangle^*}{4k_0 L}, \quad (10)$$

with \mathbb{S}_{mo} defined in (9) and k_0 the radar wavenumber. The notation $\langle \dots \rangle$ stands for the ensemble average. In this numerical approach, a Thorsos beam [27] of parameter $g = L/3$ (with L the effective illuminated length, that is the total length of the sea surface here) is considered to illuminate the generated sea surface. This beam is a tapered plane wave with a Gaussian shape. The tapering is used to reduce the incident field to near zero at the edges of the generated sea surface and so, to reduce the potential edge effects to a negligible level.

SSA1 provides a smooth transition from the geometric-optics regime (near-nadir incident angles) to the Bragg scattering regime (moderate incident angles) [28]. Therefore, by comparing the two models, one can ensure the applicability of the Bragg theory in this experiment. To do so, the wavenumber spectrum derived in subsection V-B is used to compute both the BNRCS from SPM1 (7) and the one from SSA1 (10) along the incident angle track. About the SSA1, computing the BNRCS requires a set of sea water surface elevations $\eta(r)$. Indeed, the ensemble average in (10) is performed over a set of generated sea water surface elevations, whereas the BNRCS from SPM1 only requires the measured wavenumber height clean sea water surface spectrum. This set is obtained from S_k thanks to the spectral method described by Tsang et al. [29]. Fig. 9 plots the monostatic BNRCS calculated from



(a) Radar Frequency: 8 GHz



(b) Radar Frequency: 24 GHz

Fig. 9. Monostatic BNRCS calculated from the estimated wavenumber height sea water surface spectrum for the surface state $\sigma_h = 1.09$ cm in VV (red color) and HH (blue color) polarizations. Two models are compared: SSA1 in continuous line (from a set of 200 surface realizations) and SPM1 in dashed line. The sea water dielectric constant is estimated from the Meissner and Wentz model [30].

the estimated wavenumber height sea water surface spectrum for the surface state $\sigma_h = 1.09$ cm considering the two EM models SSA1 and SPM1. Either for 8 GHz (in Fig. 9a) or for 24 GHz (in Fig. 9b), the two modeled BNRCS are merged (or very close) whatever the polarization and the incident angle. Therefore, since the SPM1 is a low-frequency method and the highest measured sea water surface state is displayed here, the Bragg scattering mechanism can be applied whatever the polarization (VV or HH), the frequency band (X-, Ku- or K-band), the sea water surface state (below $\sigma_h = 1.09$ cm) and the incident angle. This exercise demonstrates that Bragg scattering regime is established in the conditions of the experimentation.

D. Wave Damping Ratio Model

By applying the Bragg scattering theory, the EM damping ratio β can be linked to the wave damping ratio y_s . Indeed from (7),

$$\beta = \frac{\sigma_c}{\sigma_p} = \frac{S_k(k_B)}{\psi_k(k_B)}, \quad (11)$$

with ψ_k the wavenumber height contaminated sea water surface spectrum. Here, the oil dielectric impact is neglected in the kernel $\mathbb{B}(k_0, \theta)$. Indeed, oils are dielectric media with low relative permittivity and low loss factor. At microwave frequencies, the average relative permittivity ε' ranges between 2.2 and 2.3 and the loss factor ε'' is about 0.01 [31], [32]. Then, the relative penetration depth δ ,

$$\delta = \frac{\lambda_0}{\pi\sqrt{2} [\sqrt{\varepsilon'^2 + \varepsilon''^2} - \varepsilon']^{\frac{1}{2}}}, \quad (12)$$

with λ_0 the radar wavelength, is plotted in Fig. 10 along X-,Ku- and K-band ($\varepsilon' = 2.25$ and $\varepsilon'' = 0.01$). The minimum penetration depth is about 60 cm and remains much greater than the studied oil slick thickness, that is much less than 1 mm. Moreover, considering the two-layers Fresnel reflection coefficients $\Gamma_{A/W}$ rather than the equivalent three-layers ones $\Gamma_{A/O/W}$ leads to a minor error as depicted in Fig. 11. The maximum absolute Fresnel reflection coefficients error $|\Gamma_{A/W} - \Gamma_{A/O/W}|$ is about 0.5 dB with an oil film thickness equal to 1 mm. Therefore, the oil slick has a very low impact on the loss of EM energy and the dielectric influence can be ignored as a first approximation. The ratio β in (11) is equal to the wave damping ratio y_s defined for monomolecular films as [12]

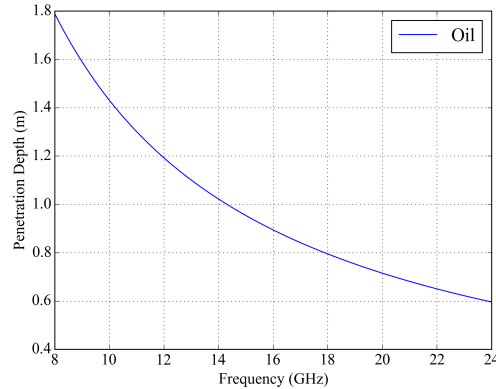


Fig. 10. Oil penetration depth versus the radar frequency.

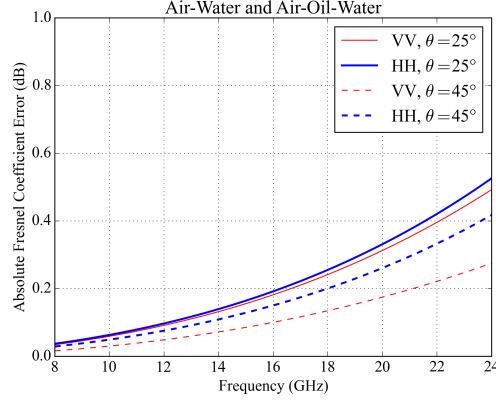


Fig. 11. Absolute Fresnel reflection coefficient error versus the radar frequency considering an oil film thickness of 1 mm in VV (red) and HH (blue) polarizations. The oil relative permittivity is 2.25 and the oil loss factor is 0.01. The sea water dielectric constant is computed from the Meissner and Wentz model [30]. Two incident angles are studied: 25° in continuous line and 45° in dashed line.

$$y_s(f) = \frac{1}{1 - F + F/y(f)}, \quad (13)$$

with F the fractional filling factor and

$$y(f) = \frac{1 \pm 2\varphi + 2\varphi^2 - X + Y(X + \varphi)}{1 \pm 2\varphi + 2\varphi^2 - 2X + 2X^2}, \quad (14)$$

with

$$\varphi = \left(\frac{\omega_D}{2\omega}\right)^{\frac{1}{2}} \quad X = \frac{E_0 k^2}{\rho(2\nu\omega^3)^{\frac{1}{2}}} \quad Y = \frac{E_0 k}{4\nu\rho\omega}, \quad (15)$$

dimensionless quantities and

$$f = \frac{\omega(k)}{2\pi}, \quad (16)$$

the dispersion relationship from (3). ω_D is a characteristic pulsation related to intermolecular forces, E_0 is the elasticity modulus, $\rho = 1.026 \cdot 10^3 \text{ kg/m}^3$ the sea water density, $\nu = 1.189 \cdot 10^{-6} \text{ m}^2/\text{s}$ the sea water kinematic viscosity [12]. A plus sign in (14) refers to soluble film, a minus to insoluble film. In this experiment, the oil films are considered insoluble. This expression does not consider the layer thickness and so, it has to be applied to thin-mono-layer problem; this is a relevant approach in the suggested experimental context. Therefore, an analytical expression of the EM damping ratio is established by considering the Bragg scattering mechanism.

E. Cost Function minimization

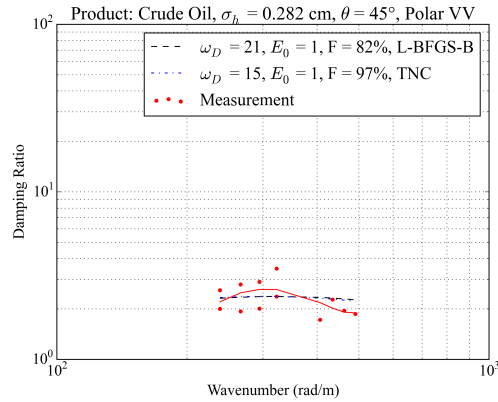
The wave damping ratio y_s in (13) can be correlated to the measured one to extract the characterization parameters of the illuminated oil slick, that are the characteristic pulsation ω_D , the elasticity modulus E_0 and the fractional filling factor F . To do so, the minimization of the cost function $C(\omega_D, E_0, F)$ is undertaken, with

$$C(\omega_D, E_0, F) = \sum_{i=0}^{N-1} \|y_s(k_i) - \beta(k_i)\|^2, \quad (17)$$

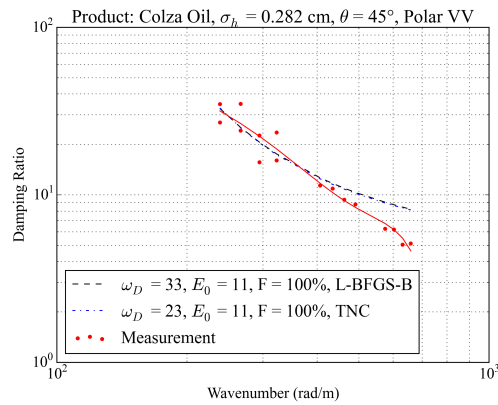
where $\|\cdot\cdot\cdot\|^2$ is the Euclidean distance and β the measured damping ratio at the Bragg wavenumber k_i (6). N measured damping ratios are available corresponding to N different radar frequencies over X-, Ku- and K-bands for a fixed incident angle. Here, the wave damping ratio y_s is written as a function of the wavenumber and not of the frequency; this is possible thanks to the dispersion relationship in (16). The minimization process is operated thanks to the Python language package *optimize* from *SciPy* providing constrained minimization of multivariate scalar functions by using two different methods: *L-BFGS-B* and *TNC*. *L-BFGS-B* is a limited-memory algorithm for solving large nonlinear optimization problems subject to simple bounds on the variables [33]. *TNC* uses a truncated Newton algorithm to minimize a function with variables subject to bounds thanks to gradient information [34]. The minimization process is constrained to ensure physical solutions [12], [14], [15], [16], [35], then ω_D is varying between 1 and 40 rad/s, the variable E_0 ranges from 1 to 50 mN/m and F from 0 to 1.

VI. RESULTS

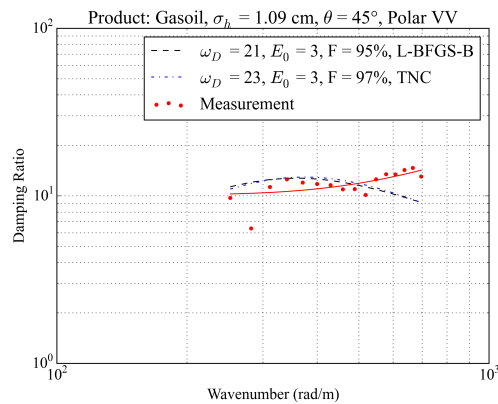
The inversion process –introduced in V-E– is applied to the measured damping ratios to estimate the parameters of the illuminated oil slick. This strategy is successively used on the three studied products –crude oil, gasoil and colza oil– considering the set of recorded data (by regarding polarization, surface state and incident angle). Fig. 12 shows the wave damping ratios (13) from the estimated parameters after the cost function minimization (17) compared to the measured ones. Both retrieved wave damping ratios are in good agreement with the measured ratios. In Fig. 12a, the estimated elasticity modulus E_0 is 1 mN/m. Typically, this value stands for mineral oil slicks and not biogenic ones ($E_0 < 10$ mN/m) [35] and so, is in agreement with a crude oil slick. Similarly, 11 mN/m in Fig. 12b matches with the value of a biogenic film –and so of a colza oil slick– and 3 mN/m in Fig. 12c agrees with a mineral oil slick. Then, in these plots, the introduced method makes a nature-related identification possible by distinguishing biogenic films from mineral ones. TABLE II presents all the retrieved product parameters $\{\omega_D, E_0, F\}$ in $\{\text{rad/s, mN/m, dimensionless quantity}\}$ after applying the cost function minimization (17). The first column displays the experimental conditions, that are the surface state through the standard deviation of the surface height σ_h in cm, the incident angle θ in degree and the polarization VV or HH. At last, the symbol \emptyset means non-acquired data. Here, the focus is on the elasticity modulus and on the fractional filling factor, the two main parameters to characterize an oil slick (by following the criterion $E_0 < 10$ mN/m in a presence of a mineral oil slick). About the crude oil and the gasoil, the identification of the mineral property (through E_0) is achieved whatever the polarization and the surface state (only for gasoil). The colza oil case is trickier. Indeed, the assessment of the biogenic aspect is realized at the lowest surface state only, the two other surface states induce a mineral characterization from the applied method. Seemingly, at higher surface state and unlike the gasoil slick, the colza oil slick shifts from an homogeneous film to an inhomogeneous one and so moves from a film to an emulsion. Then, the considered modeling of the damping ratio is not sufficient to describe the overall phenomenon. This result is consistent with Romano [36] who observed biogenic films only at wind speeds below 5 m/s, suggesting that these films are mixed and dissolved in the sea water under the action of breaking waves and thus, disappeared from the sea surface. Furthermore, the fractional filling factor –either for colza oil or for gasoil– decreases with increasing sea water surface state. For example, for colza oil, it varies from 1.0 for $\sigma_h = 0.282$ cm to 0.86 for $\sigma_h = 1.09$ cm assuming a correlation between



(a) Crude Oil



(b) Colza Oil

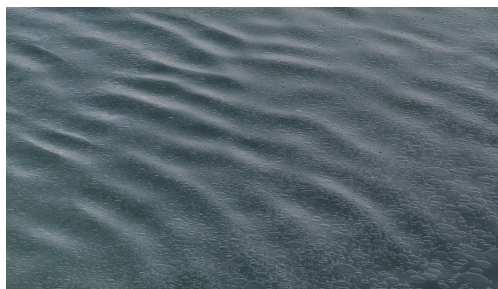


(c) Gasoil

Fig. 12. Damping ratios calculated from oil slicks considering a given sea water surface state in VV polarization for an incident angle of 45° . The data points (red dots) are fitted by a third-degree polynome (red line). The dashed lines are the damping ratios obtained from the minimization process (black dashed line: L-BFGS-B method, blue dotted line: TNC method).

the fractional filling factor and the surface state. Presumably, the emulsion behaviour for colza oil slick at higher surface state implies a change from a surface problem to a volume one, that is a loss of product on the surface. About the gasoil at higher surface state, seemingly, the slick uniformity is broken, leading to smaller gasoil slicks

into the radar footprint. The colza behaviour is displayed in Fig. 13 for $\sigma_h = 0.282$ cm (13a) and $\sigma_h = 1.09$ cm (13b). As previously suggested, in 13a, the colza oil film is homogeneous with large oil bubbles while in 13b the film becomes inhomogeneous and the bubbles are hardly distinguished from the sea water.



(a) $\sigma_h = 0.282$ cm



(b) $\sigma_h = 1.09$ cm

Fig. 13. Photographs from the colza-oil-covered sea water surface.

VII. SUMMARY AND OUTLOOKS

Measurements in a wind-wave pool and modeling of the wave damping ratio from oil-covered sea water surface were combined to elaborate an *a priori* oil characterization methodology over multi-frequency radar data. About physical models and well-controlled experiments, an extended description of the sea water surface is proposed through both the statistical properties of the surface and the radar backscatter. The characterization methodology is based on the minimization of the cost function correlating the values given by a physical model of the wave damping ratio and the measured ones. The chosen model implies the Bragg scattering mechanism. To prove the latter, a frequency-to-wavenumber conversion from the surface elevation measurements has been developed in order to get the wavenumber height sea water surface spectrum. This spectrum is then used to compute the modeled BNRCS from SSA1 and SPM1, demonstrating the Bragg mechanism validity in our experimental conditions. The oil characterization approach is reliable to identify the mineral-or-biogenic origin for low sea water surface state (≈ 0.282 cm in standard deviation of the surface height) for the crude oil, the colza oil and the gasoil. At higher sea water surface state ($\sigma_h = 0.684$ cm and $\sigma_h = 1.09$ cm), the methodology does not retrieve the biogenic criterion for colza oil (and so could be an error-raising vector in a blind inversion process) but succeeds in any of both mineral oil cases. In an operational context, this ambiguity at higher sea state could be vanished by monitoring the detected oil slick along different meteorological conditions. At last, the behaviour of the oil coverage over the sea

TABLE II
SYNTHESIS OF INVERTED OIL CHARACTERIZATION PARAMETERS AND ASSOCIATED CONDITIONS

$\{\sigma_h, \theta, \text{Polar}\}$ σ_h in cm	Crude Oil $\{\omega_D, E_0, F\}$	Colza Oil	Gasoil
$\{0.282, 45^\circ, \text{VV}\}$	L-BFGS-B: {21, 1, 0.82} TNC: {15, 1, 0.97}	L-BFGS-B: {33, 11, 1.0} TNC: {23, 11, 1.0}	\emptyset
$\{0.282, 45^\circ, \text{HH}\}$	L-BFGS-B: {21, 1, 0.86} TNC: {15, 1, 0.93}	L-BFGS-B: {21, 17, 1.0} TNC: {22, 17, 1.0}	\emptyset
$\{0.684, 45^\circ, \text{VV}\}$	\emptyset	L-BFGS-B: {40, 3, 0.91} TNC: {22, 3, 0.92}	L-BFGS-B: {40, 3, 0.98} TNC: {40, 3, 0.98}
$\{0.684, 45^\circ, \text{HH}\}$	\emptyset	L-BFGS-B: {40, 1, 1.0} TNC: {26, 2, 0.91}	L-BFGS-B: {40, 3, 0.97} TNC: {40, 3, 0.97}
$\{0.684, 25^\circ, \text{VV}\}$	\emptyset	\emptyset	L-BFGS-B: {22, 4, 0.99} TNC: {40, 5, 0.98}
$\{0.684, 25^\circ, \text{HH}\}$	\emptyset	\emptyset	L-BFGS-B: {40, 5, 0.98} TNC: {40, 5, 0.98}
$\{1.09, 45^\circ, \text{VV}\}$	\emptyset	L-BFGS-B: {40, 3, 0.91} TNC: {40, 3, 0.91}	L-BFGS-B: {21, 3, 0.95} TNC: {23, 3, 0.97}
$\{1.09, 45^\circ, \text{HH}\}$	\emptyset	L-BFGS-B: {40, 3, 0.87} TNC: {40, 3, 0.87}	L-BFGS-B: {40, 3, 0.91} TNC: {23, 3, 0.93}
$\{1.09, 25^\circ, \text{VV}\}$	\emptyset	L-BFGS-B: {21, 5, 0.86} TNC: {21, 5, 0.86}	\emptyset
$\{1.09, 25^\circ, \text{HH}\}$	\emptyset	L-BFGS-B: {21, 6, 0.86} TNC: {10, 6, 0.87}	\emptyset

water surface is further explained by noticing that the fractional filling factor decreases when increasing the sea water surface state for both the colza oil and the gasoil.

This study shows that accurate multi-frequency radar measurement could be a relevant and reliable mean to characterize an oil-covered sea surface. Then, in future works, this oil characterization methodology will be applied on other dataset acquired in a maritime environment to further test the resilience of the strategy by considering an operational context and numerous oil slicks. At last, this study is focused on thin oil films and could be improved by considering the oil film thickness to perform an oil quantification [37].

APPENDIX A NEAR-FIELD CONFIGURATION

As explained in section II, in X-band configuration the radar system operates in the limit of the Fresnel zone. This issue does not occur with higher frequencies –like 23.5 GHz for example– and the radar measurements are then achieved in the near-field region. Fig. 14 plots the normalized incoherent field with respect to the radar range (cf. Fig. 1b) considering a clean sea water surface of sea state $\sigma_h = 0.282$ cm with an incident angle $\theta = 45^\circ$ in VV polarization. The three displayed fields result from three different radar frequencies; 8.5 GHz, 11.5 GHz and 23.5 GHz. The radar beam footprints projected on the sea water surface and observed along the radar range are similar whatever the frequencies. This result shows that no divergence of the beam occurred in X-band configuration and all of the radar measurements are therefore realized in the near-field region.

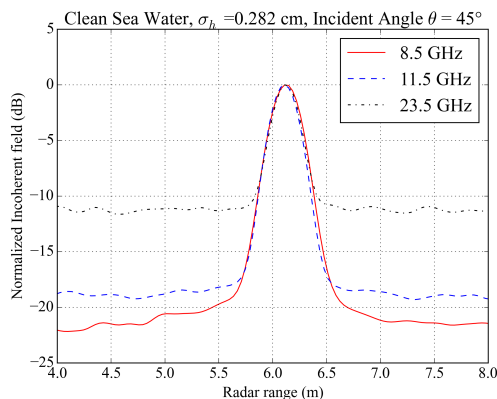


Fig. 14. Normalized incoherent field versus the radar range considering a clean sea water surface of sea state $\sigma_h = 0.282$ cm with an incident angle $\theta = 45^\circ$ in VV polarization. Three radar frequencies are considered: 8.5 GHz (red line), 11.5 GHz (blue dashed line) and 23.5 GHz (black dotted line).

ACKNOWLEDGMENT

Research presented in this paper is part of the NAOMI (New Advanced Observation Method Integration) Project funded by TOTAL (the French petroleum company) and ONERA (the French Aerospace Lab). The authors would like to thank all people involved in this project, and especially Pierre-Yves Foucher, Veronique Miegbielle and Dominique Dubucq for supporting this work. The authors are very grateful to the CEDRE (Centre of Documentation,

Research and Experimentation on Accidental Water Pollution) for allowing us to achieve the Oil-on-Water exercise, which was carried out during 25-29 September and 9-13 October, 2017.

REFERENCES

- [1] M. Fingas and C. Brown, "Review of oil spill remote sensing," *Marine Pollution Bulletin*, vol. 83, no. 1, pp. 9–23, 2014.
- [2] I. Leifer, W. J. Lehr, D. Simecek-Beatty, E. Bradley, R. Clark, P. Dennison, Y. Hu, S. Matheson, C. E. Jones, B. Holt, M. Reif, D. A. Roberts, J. Svejkovsky, G. Swayze, and J. Wozencraft, "State of the art satellite and airborne marine oil spill remote sensing : Application to the BP Deepwater Horizon oil spill," *Remote Sensing of Environment*, vol. 124, pp. 185–209, 2012.
- [3] R. Jatiault, D. Dhont, L. Loncke, and D. Dubucq, "Monitoring of natural oil seepage in the Lower Congo Basin using SAR observations," *Remote Sensing of Environment*, vol. 191, pp. 258–272, 2017.
- [4] M. Gade and W. Alpers, "Using ERS-2 SAR images for routine observation of marine pollution in European coastal waters," *Science of The Total Environment*, vol. 237-238, pp. 441–448, 1999.
- [5] F. Girard-Ardhuin, G. Mercier, F. Collard, and R. Garello, "Operational Oil-Slick Characterization by SAR Imagery and Synergistic Data," *IEEE Journal of Oceanic Engineering*, vol. 30, no. 3, pp. 487–495, 2005.
- [6] O. Garcia-Pineda, B. Zimmer, M. Howard, W. Pichel, X. Li, and I. R. Macdonald, "Using SAR images to delineate ocean oil slicks with a texture-classifying neural network algorithm (TCNNA)," *Canadian Journal of Remote Sensing*, vol. 35, no. 5, pp. 411–421, 2009.
- [7] B. Holt and C. Jones, "Detection of marine slicks with SAR: Scientific and experimental legacy of werner alpers, his students and colleagues," in *International Geoscience and Remote Sensing Symposium (IGARSS)*, Fort Worth, Texas, 2017, pp. 1480–1483.
- [8] A. H. Solberg, "Remote Sensing of Ocean Oil-Spill Pollution," *Proceedings of the IEEE*, vol. 100, no. 10, pp. 2931–2945, 2012.
- [9] S. Angelliaume, P. C. Dubois-fernandez, C. E. Jones, B. Holt, B. Minchew, E. Amri, and V. Miegbielle, "SAR Imagery for Detecting Sea Surface Slicks : Performance Assessment of Polarization- Dependent Parameters," *IEEE Transactions on Geoscience and Remote Sensing*, vol. PP, no. 99, pp. 1–21, 2018.
- [10] S. Angelliaume, X. Ceamanos, F. Viallefont-robinet, R. Baqué, P. Déliot, and V. Miegbielle, "Hyperspectral and Radar Airborne Imagery over Controlled Release of Oil at Sea," *Sensors*, vol. 17, 2017.
- [11] W. Alpers and H. Hühnerfuss, "Radar Signatures of Oil Films Floating on the Sea Surface and the Marangoni Effect," *Journal of Geophysical Research: Oceans*, vol. 93, no. C4, pp. 3642–3648, 1988.
- [12] P. P. Lombardini, B. Fiscella, P. Trivero, C. Cappa, and W. Garrett, "Modulation of the Spectra of Short Gravity Waves by Sea Surface Films: Slick Detection and Characterization with a Microwave Probe," *Journal of Atmospheric and Oceanic Technology*, vol. 6, pp. 882–890, 1989.
- [13] H. Hühnerfuss, A. Gericke, W. Alpers, R. Theis, V. Wismann, and P. A. Lange, "Classification of sea slicks by multifrequency radar techniques : New chemical insights and their geophysical implications," *Journal of Geophysical Research*, vol. 99, no. C5, pp. 9835–9845, 1994.
- [14] M. Gade, W. Alpers, H. Hühnerfuss, and P. A. Lange, "Wind wave tank measurements of wave damping and radar cross sections in the presence of monomolecular surface films," *Journal of Geophysical Research*, vol. 103, no. C2, pp. 3167–3178, 1998.
- [15] M. Gade, W. Alpers, H. Hühnerfuss, H. Masuko, and T. Kobayashi, "Imaging of biogenic and anthropogenic ocean surface films by the multifrequency/multipolarization SIR-C/X-SAR," *Journal of Geophysical Research: Oceans*, vol. 103, no. C9, pp. 18,851–18,866, 1998.
- [16] S. A. Ermakov, "Possibilities of Identification of Oil Films Using Radar Probing of the Sea Surface," in *US/EU-Baltic International Symposium*, 2008, pp. 1–6.
- [17] I. Sergievskaya and S. Ermakov, "On Wave Damping due to Oil Films," in *US/EU-Baltic International Symposium*, 2008, pp. 8–13.
- [18] L. J. Foged, M. A. Saporetta, E. Jørgensen, T. Voigt, F. Calvano, and D. Tallini, "Measurement and Simulation of Reflector Antenna," in *2015 9th European Conference on Antennas and Propagation (EuCAP)*, 2015.
- [19] O. Nwogu, "Maximum entropy estimation of directional wave spectra from an array of wave probes," *Applied Ocean Research*, vol. 11, no. 4, pp. 176–182, 1990.
- [20] O. Boisot, S. Pioch, C. Fatras, G. Caulliez, A. Bringer, P. Borderies, J.-C. Lalaurie, and C.-A. Guérin, "Ka-band backscattering fromwater surface at small incidence: A wind-wave tank study," *Journal of Geophysical Research: Oceans*, pp. 1–25, 2015.
- [21] O. Boisot, A. Laiba, J.-C. Lalaurie, and C.-A. Guérin, "Dynamical Properties of Sea Surface Microwave Backscatter at Low-Incidence: Correlation Time and Doppler Shift," *IEEE Transactions on Geoscience and Remote Sensing*, vol. PP, pp. 1–11, 2016.

- [22] T. M. Elfouhaily and C.-A. Guérin, “A critical survey of approximate scattering wave theories from random rough surfaces,” *Waves in Random Media*, vol. 7174, no. October, 2004.
- [23] A. G. Voronovich, “Small-slope approximation in wave scattering by rough surfaces,” *Journal of Experimental and Theoretical Physics*, vol. 62, pp. 65–70, 1986.
- [24] C. Bourlier, N. Déchamps, and G. Berginc, “Comparison of asymptotic backscattering models (SSA, WCA, and LCA) from one-dimensional Gaussian ocean-like surfaces,” *IEEE Transactions on Antennas and Propagation*, vol. 53, no. 5, pp. 1640–1652, 2005.
- [25] T. M. Elfouhaily, B. Chapron, K. Katsaros, and D. Vandemark, “A unified directional spectrum for long and short wind-driven waves,” *Journal of Geophysical Research: Oceans*, vol. 102, no. C7, pp. 15 781–15 796, 1997.
- [26] T. Hara, E. J. Bock, and D. Lyzenga, “In situ measurements of capillary-gravity wave spectra using a scanning laser slope gauge and microwave radars,” *Journal of Geophysical Research*, vol. 99, no. C6, pp. 12,593–12,602, 1994.
- [27] C. Bourlier, N. Pinel, and G. Kubicke, *Method of Moments for 2D Scattering Problems: Basic Concepts and Applications*. Hoboken, USA: John Wiley & Sons, Inc., 2013.
- [28] A. G. Voronovich and V. U. Zavorotny, “Theoretical model for scattering of radar signals in Ku- and C-bands from a rough sea surface with breaking waves,” *Waves in Random Media*, vol. 11, no. 3, pp. 247–270, 2001.
- [29] L. Tsang, J. Au Kong, K.-H. Ding, and C. O. Ao, *Scattering of Electromagnetic Waves: Numerical Simulations*. John Wiley & Sons, Inc., 2002.
- [30] T. Meissner and F. J. Wentz, “The Complex Dielectric Constant of Pure and Sea Water From Microwave Satellite Observations,” *IEEE Transactions on Geoscience and Remote Sensing*, vol. 42, no. 9, pp. 1836–1849, 2004.
- [31] T. Friisø, Y. Schildberg, O. Rambeau, T. Tjomsland, and J. Sjøblom, “Complex permittivity of crude oils and solutions of heavy crude oil fractions,” *Journal of Dispersion Science and Technology*, vol. 19, no. 1, pp. 93–126, 1998.
- [32] K. Folgerø, “Bilinear calibration of coaxial transmission / reflection cells for permittivity measurement of low-loss liquids,” *Measurement Science and Technology*, vol. 7, no. 9, pp. 1260–1269, 1996.
- [33] C. Zhu, R. H. Byrd, P. Lu, and J. Nocedal, “Algorithm 778 : L-BFGS-B : Fortran Subroutines for Large-Scale Bound- Constrained Optimization,” *ACM Transactions on Mathematical Software*, vol. 23, no. 4, pp. 550–560, 1997.
- [34] S. G. Nash, “Newton-Type Minimization via the Lanczos Method,” *SIAM Journal of Numerical Analysis*, vol. 21, no. 4, pp. 770–788, 1984.
- [35] N. Pinel and C. Bourlier, “Modeling of radar scattering from oil films,” in *International Radar Conference, Bordeaux : France (2009)*, no. 1, Bordeaux, 2009, pp. 1–6.
- [36] J.-C. Romano, “Sea-surface slick occurrence in the open sea (Mediterranean, Red Sea, Indian Ocean) in relation to wind speed,” *Deep Sea Research Part I: Oceanographic Research Papers*, vol. 43, no. 4, pp. 411–423, 1996.
- [37] O. Boissot, S. Angelliaume, C.-A. Guérin, and V. Miegébielle, “Introduction to oil quantification on sea surface from microwaves polarimetric SAR measurements,” in *Geoscience and Remote Sensing Symposium (IGARSS), 2017 IEEE International*, 2017.